AIAA JOURNAL
Vol. 40, No. 3, March 2002

Experimental and Theoretical Study of Gust Response for High-Aspect-Ratio Wing

Deman Tang* and Earl H. Dowell†
Duke University, Durham, North Carolina 27708-0300

A nonlinear response analysis of a high-aspect-ratio wing aeroelastic model excited by gust loads is presented along with a companion wind-tunnel test program. For the wind-tunnel tests, a high-aspect-ratio wing aeroelastic experimental model with a slender body at the tip has been constructed, and a rotating slotted cylinder gust generator has been used to generate a gust excitation field. A LabVIEW 5.1 measurement and analysis system is used to measure the gust response, flutter boundary, and limit-cycle oscillation behavior. Structural equations of motion based on a nonlinear beam theory are combined with the ONERA aerodynamic stall model to study the effects of geometric structural nonlinearity and steady angle of attack on nonlinear gust response of high-aspect-ratio wings. Also a dynamic perturbation analysis about a nonlinear static equilibrium is used to determine the small perturbation flutter boundary. The fair to good quantitative agreement between theory and experiment demonstrates that the present analysis method has reasonable accuracy.

Nomenclature

C_d	=	section drag coefficient
C_l	=	section lift coefficient
C_m	=	section torsional moment coefficient
C_ξ	=	structural damping
$c, \bar{c}$	=	wing chord and dimensionless chord, c/L
c_{SB}	=	chord of slender body
dD, dL	=	section drag and lift forces
dF_v, dF_w	=	section chordwise and vertical component forces
dM_x	=	section pitch moment about elastic axis
dM_0	=	section pitch moment about one-quarter chord
E	=	modulus of elasticity
e	=	section mass center from elastic axis
G	=	shear modulus
g	=	gravitational constant
I_1, I_2	=	vertical and chordwise area moments
J	=	torsional stiffness constant
K_m	=	wing mass radius of gyration
L	=	wing span
M	=	tip mass of the wing
m	=	mass per unit length of the wing
N_a	=	number of aerodynamic elements
N_s	=	total number of structural modes
t	=	time
U	=	freestream velocity
V_j, W_j	=	generalized coordinates for bending
v	=	chordwise bending deflection
w	=	vertical bending deflection
x	=	position coordinate along wing span
y_{ac}	=	distance of aerodynamic center of airfoil section from elastic axis
α	=	wing section angle of attack
α_G	=	gust angle of attack
Δ_l	=	dimensionless width of lth spanwise aerodynamic element
θ_0	=	steady angle of attack at root section
ρ	=	air density
Φ_j	=	generalized coordinates for torsion
ϕ	=	twist about deformed elastic axis
ω	=	gust frequency $\omega_{\phi j}$, jth torsional natural frequency of wing
ω_{vj}	=	jth chordwise natural frequency of wing
ω_{wj}	=	jth vertical natural frequency of wing
$'$	=	$d(\,)/dx$
$\dot{}$	=	$d(\,)/dt$

Received 22 November 2000; revision received 25 June 2001; accepted for publication 2 September 2001.

*Research Associate Professor, Department of Mechanical Engineering and Materials Science. Member AIAA.

†J. A. Jones Professor, Department of Mechanical Engineering and Materials Science. Fellow AIAA.

Introduction

MANY authors have studied the aeroelastic stability and response of an aircraft with a high-aspect-ratio wing from subsonic to supersonic flow. Linear beam theory is often used to simplify the wing structural model; however, a geometric structural nonlinearity may arise from the coupling between elastic flap bending w, chordwise bending v, and torsion ϕ for very high-aspect-ratio wings typical of long-endurance, high-altitude uninhabited air vehicles. The effect of the large static preflutter deformation on the flutter boundary, limit-cycle oscillation (LCO) response, and most significantly and primarily gust response is studied here. Previous work has been primarily concerned with flutter and LCO. The results provide additional insight with respect to the contribution of structural nonlinear coupling to the aeroelastic stability and response of high-aspect-ratio wings.

Following Refs. 1–5, an experimental and theoretical study on flutter and LCOs of high-aspect-ratio wings has been reported in Ref. 6. An experimental high-aspect-ratio wing aeroelastic model with a tip slender body was constructed, and a wind-tunnel test was conducted to measure the static aeroelastic response, flutter, and LCOs.[6] Large static preflutter deformations in the vertical or torsional direction were created by the gravity loading on the horizontally mounted wing and a tip slender body and also by a steady angle of attack at the wing root, which creates a static aerodynamic load on the wing. The experimental results[6] largely validate the theoretical results of earlier studies.[3–5] In particular, a hysteresis phenomenon was found in both the theoretical analysis and experimental observation of the nonlinear aeroelastic system.

Following the work of Ref. 6, in the present paper we develop a mathematical model and computational code in the time domain to calculate the nonlinear gust response of an aircraft with a high-aspect-ratio wing at low subsonic flow speeds. Different from the wing experimental model tested in Ref. 6, the present wing model is mounted vertically to eliminate gravity effects. Large static preflutter deformations in the flapwise or torsional direction are, thus, only created by a steady angle of attack at the wing root. Sinusoidal and linear frequency sweep gust loads are used in both the

theoretical prediction and wind-tunnel test. Structural equations of motion based on a nonlinear beam theory are combined with the ONERA aerodynamic stall model to study the effects of geometric structural nonlinearity and steady angle of attack on nonlinear gust response of high-aspect-ratio wings. Also a dynamic perturbation analysis about a nonlinear static equilibrium is used to determine the small perturbation flutter boundary.

To validate the theoretically predicted gust response characteristics of the high-aspect-ratio wing, an experimental investigation has been carried out in the Duke wind tunnel using a rotating slotted cylinder (RSC) gust generator based on a concept of Reed (see Ref. 7) and a LabVIEW 5.1 measurement and analysis system to measure the gust response and LCO deflections of the wing model. The results may be helpful in better understanding physically the nonlinear aeroelastic response of a high-aspect-ratiowing model to gust loads and assessing the accuracy of the present (or another) mathematical model and computational code.

Experimental Wing Model and Measurements

The experimental model includes two parts: a high-aspect-ratio wing with a slender body at the tip and a root support mechanism. The wing is rectangular, untwisted, and flexible in the flap w, lag v, and torsional ϕ directions (see Fig. 1 for a schematic of the model). The wing is constructed from a precision ground flap steel spar with mass uniformly distributed along the wing span. The spar is 45.7 cm in length, 1.27 cm in width, and 0.127 cm in thickness. It is inserted tightly into the wing root mechanism. To reduce torsional stiffness, the spar has multiple thin flanges along the span. The flange width is 0.127 cm, and it is 0.318 cm deep. There are 2×33 flanges uniformly and symmetrically distributed along the wing span and centerline of the spar. There are 18 pieces of NACA 0012 airfoil plate uniformly distributed along the span. The pieces of the airfoil plate are made of aluminum alloy with 0.1 in. thickness. A precision aerodynamic contour of the wing model is obtained. Each airfoil plate has a slot 1.27 cm in width and 0.127 cm in thickness at the symmetry line. The spar is inserted through these airfoil plate slots, and they are permanently bonded together. Each space between two airfoil plates is filled with a light wood (balsa) covering the entire chord and span, which provides the aerodynamic contour of the wing. This wood provides a slight additional mass and a small addition to the bending and torsion stiffness.

A slender body is attached to the elastic axis of the wing tip. The slender body is an aluminum bar, 0.95 cm in diameter and 10.16 cm in length. A paraboloidal forebody and an aftbody with 1.14 cm length are fixed to two ends of the bar. The forebody and aftbody are made of brass. The geometry of the paraboloidal forebody is described as follows:

$$R/R_0 = \bar{y}^2, \qquad \bar{y} = 0 \longrightarrow 1$$

The slender body is symmetrical and is designed to provide enough torsional inertia to reduce the natural torsional frequency sufficiently to induce flutter in the velocity range of the wind tunnel.

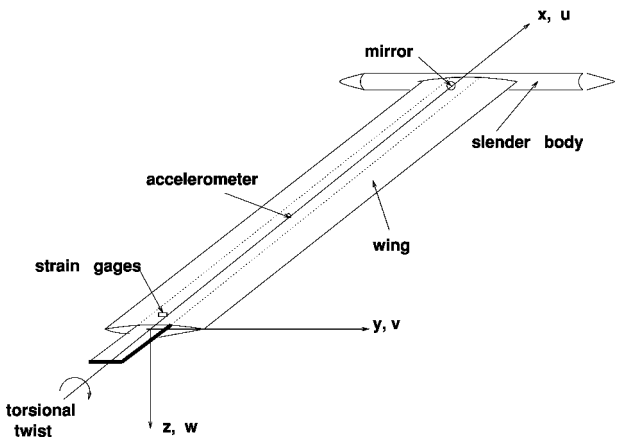

Fig. 1 Physical representation of wing model.

Fig. 2 Experimental model and gust generator in the wind tunnel.

The root support mechanism is a socket that allows a change of the steady angle of attack at the root. The root socket is mounted to the midpoint of the top wind-tunnel wall as shown in Fig. 2, which is a photograph of the aeroelastic wing model with a gust generator in the wind tunnel.

Axial strain gauges for bending modes and a 45-deg oriented strain gauge for torsional modes were glued to the root spar to measure the bending–torsional deflections of the wing. Signals from the strain gauges were conditioned and amplified before their measurement through a gauge conditioner and a low-pass filter. A microaccelerometer is mounted at midspan of the wing. The output signals from these transducers are directly recorded on a computer with data acquisition and analysis software, LabVIEW 5.1.

A helium–neon laser with 0.8-mW randomly polarized and wavelength 633 nm is mounted on the top of the tunnel. The top of the tunnel is made of a 1.27-cm-thick glass plate. A 1.27-cm-diam mirror, is fixed on the tip of the wing. A mirror deflection technique is used to determine the tip twist and tip flap bending slope of the wing. A point produced by the reflected light source is marked on a readout grid paper placed on the top of the wind tunnel when the wing is undeflected. The readout grid paper is calibrated with respect to tip flap and twist deflections before the test. The displacement of the reflected light source point is then determined as the flow velocity is varied.

The gust was created by placing an RSC behind a fixed airfoil upstream of the wing model. For details of the gust generator configuration and control, see Ref. 7.

All flutter, LCO, and gust response tests were performed in the Duke University low-speed wind tunnel and tunnel measurement system. The wind tunnel is a closed circuit tunnel with a 0.7×0.53 m^2 test section and a length of 1.52 m. The maximum airspeed attainable is 89.3 m/s.

The basic parameters of the experimental wing model were obtained from standard static and vibration tests and are listed in Table 1.

State-Space Equations

Structural Model

According to the Hodges–Dowell equations,[1] for a uniform, untwisted elastic wing, neglecting cross section warping, the equations of motion may be written as

$$EI_2 v'''' + (EI_2 - EI_1)[\phi(w)'']'' + m\ddot{v} + C_\xi \dot{v} + (M\ddot{v} + I_z\ddot{v}')\delta(x-L) + v_{mg} = \frac{\mathrm{d}F_v}{\mathrm{d}x} + \Delta F_v \tag{1}$$

$$EI_1(w)'''' + (EI_2 - EI_1)(\phi v'')'' + m\ddot{w} - me\ddot{\phi} + C_\xi \dot{w} + (M\ddot{w} + I_y\ddot{w}')\delta(x-L) + w_{mg} = \frac{\mathrm{d}F_w}{\mathrm{d}x} + \Delta F_w \tag{2}$$

$$-GJ\phi'' + (EI_2 - EI_1)w''v'' + I_x\ddot{\phi}\delta(x-L) + mK_m^2\ddot{\phi} + C_\xi\dot{\phi} - me\ddot{w} = \frac{\mathrm{d}M_x}{\mathrm{d}x} + \Delta M_x \tag{3}$$

Table 1 Experimental wing model data

Properties	Value
Wing	
Span L	0.4508 m
Chord c	0.0508 m
Mass per unit length	0.2351 kg/m
Moment inertia (50% chord)	0.2056×10^{-4} kgm
Spanwise elastic axis	50% chord
Center of gravity	49% chord
Flap bending rigidity EI_1	$0.4186\ \mathrm{N \cdot m^2}$
Chordwise bending rigidity EI_2	$0.1844 \times 10^2\ \mathrm{N \cdot m^2}$
Torsional rigidity GJ	$0.9539\ \mathrm{N \cdot m^2}$
Flap structural modal damping ξ_w	0.02
Chordwise structural modal damping ξ_v	0.025
Torsional structural modal damping ξ_ϕ	0.031
Slender body	
Radius R	0.4762×10^{-2} m
Chord length c_{SB}	0.1406 m
Mass M	0.0417 kg
Moment inertia I_x	$0.9753 \times 10^{-4}\ \mathrm{kgm^2}$
Moment inertia I_y	$0.3783 \times 10^{-5}\ \mathrm{kgm^2}$
Moment inertia I_z	$0.9753 \times 10^{-4}\ \mathrm{kgm^2}$

A few general comments about Eqs. (1–3) may be in order. First, when each of these equations is multiplied by δv, δw, and $\delta\phi$, respectively, and integration is performed over the length of the beam, a variational statement may be derived. Conversely, as shown in Ref. 1, these equations may be derived from Hamilton's principle.

The vertical longitudinal displacement of the wing model is

$$u = \frac{1}{2}\int_0^x [(v')^2 + (w')^2]\,\mathrm{d}x$$

Hence, the gravitational elastic potential energy of the wing (including tip slender body) is

$$V_{mg} = \frac{1}{2}mg\int_0^L\int_0^x [(v')^2 + (w')^2]\,\mathrm{d}x\,\mathrm{d}x + \frac{1}{2}Mg\int_0^L [(v')^2 + (w')^2]\,\mathrm{d}x$$

From V_{mg}, the restoring stiffness terms v_{mg} and w_{mg} may be deduced by variational methods.

Note that in Eqs. (1–3) only the most important nonlinear terms are retained from the Hodges–Dowell equations[1] and the third- and higher-order geometrically nonlinear terms are neglected here. Also note that the geometric twist angle

$$\hat{\phi} = \phi + \int_0^x v'w''\,\mathrm{d}x$$

is considered in the aerodynamic terms. M is the tip slender body mass, I_x, I_y, and I_z are the tip mass inertial properties, θ_0 is the pitch angle or steady angle of attack at the root of this wing model, and e is the distance between mass center and wing elastic axis center. Note that Patil et al.[3] and Patil and Hodges[5] have improved these equations to allow for large deflections.

Aerodynamic Models

The aerodynamic forces include two parts. One contribution is from the wing surface, $\mathrm{d}F_w/\mathrm{d}x$, $\mathrm{d}F_v/\mathrm{d}x$, and $\mathrm{d}M_x/\mathrm{d}x$, and the other is from the slender body at the wing tip, ΔF_w, ΔF_v, and ΔM_x.

ONERA Airfoil Model

The v and w components of the aerodynamic force and the aerodynamic moment about the elastic axis x can be expressed as follows:

$$\mathrm{d}F_w = \mathrm{d}L - (\phi_\lambda - \theta_0)\,\mathrm{d}D, \qquad \mathrm{d}F_v = -\mathrm{d}D - (\phi_\lambda - \theta_0)\,\mathrm{d}L$$

$$\mathrm{d}M_x = \mathrm{d}M_0 - y_{ac}\,\mathrm{d}F_w \tag{4}$$

where

$$\mathrm{d}L = \tfrac{1}{2}\rho cU^2 C_l\,\mathrm{d}x, \qquad \mathrm{d}D = \tfrac{1}{2}\rho cU^2 C_d\,\mathrm{d}x$$

$$\mathrm{d}M_0 = \tfrac{1}{2}\rho c^2 U^2 C_m\,\mathrm{d}x, \qquad \phi_\lambda \approx \dot{w}/(U + \dot{v} + \dot{w}\theta_0)$$

$$\alpha = \hat{\phi} + \theta_0 - \phi_\lambda + \alpha_G$$

and α_G is an effective gust angle of attack.

The section aerodynamic coefficients C_l, C_d, and C_m are obtained from the original ONERA stall aerodynamic model (see Refs. 8 and 9). These airfoil relationships are combined with a strip theory assumption to determine the wing aerodynamic forces. Patil and Hodges[5] have shown the strip theory assumption is a good one for such high-aspect-ratio wings. See Refs. 5 and 6 for more details of the aerodynamic model.

Slender Body Theory

We follow Bisplinghoff et al. (Ref. 10, page 418 and the following ones) to derive the aerodynamic forces of the slender body. For details, see Ref. 6. The results are

$$\Delta F_w = \rho\left[(\ddot{w} + U\dot{\phi})\int_0^{c_{SB}} S\,\mathrm{d}y + \ddot{\phi}\int_0^{c_{SB}} S(y - y_B)\,\mathrm{d}y\right]\delta(x - L)$$

$$\Delta M_x = \rho\left[(U\dot{w} + U^2\phi)\int_0^{c_{SB}} S\,\mathrm{d}y - \ddot{w}\int_0^{c_{SB}} S(y - y_B)\,\mathrm{d}y - \ddot{\phi}\int_0^{c_{SB}} S(y - y_B)^2\,\mathrm{d}y\right]\delta(x - L) \tag{5}$$

and if we assume the slender body drag can be neglected, then

$$\Delta F_v = -(\phi_\lambda - \phi - \theta_0)\Delta F_w$$

where y is the chordwise position and $y_B \equiv y_{ea}$ is the distance from leading edge to the elastic axis of the slender body. $S \equiv$ body cross-sectional area and $S = \pi R^2$, for a circular cross-section of radius $R(y)$.

Gust Angle of Attack α_G

When we use the ONERA aerodynamic model, a key consideration is how to express the gust angle of attack for an airfoil entering a sinusoidal gust field. A generic expression of the effective gust angle of attack is

$$\alpha_G(t, \bar{y}) = \alpha_{G0}\sin(\omega t - k\bar{y})$$

where $\bar{y}$ is the nondimensional streamwise coordinate fixed on the airfoil, with the origin $\bar{y} = 0$ located at the midchord point, and k is the reduced frequency. In this paper, we assume the chordwise distribution of the gust velocity may be regarded as constant at any instant of time and equal to the gust at the midchord point. The effective gust angle of attack is, thus,

$$\alpha_G(t) = \alpha_{G0}\sin\omega t \tag{6}$$

This assumption is valid for the present experimental wing model, as shown in Ref. 11.

A continuous frequency sweep gust is also considered. It is expressed as

$$\alpha_G(t) = \alpha_{G0}\sin\{\omega_1 + [(\omega_2 - \omega_1)/2T]t\}t \tag{7}$$

where ω_1, ω_2, and T are the minimum frequency, maximum frequency, and the sweep duration, respectively.

Theoretical results for gust response are obtained using a time-marching approach. The flow velocity is below the flutter velocity for these measurements and calculations. For the strip theory, ONERA aerodynamic model, the wing is divided into 10 spanwise aerodynamic sections, this is, $N_a = 10$. The stall aerodynamic data for an NACA 0012 airfoil are used in this paper (see Ref. 9).

Structural Modal Equations

Expansions in general mode shape functions are used to obtain ordinary differential equations in terms of generalized coordinates from Eqs. (1–3). They are expressed in series form as follows:

$$\bar{v} = \sum_{j=1}^{N} V_j(t)\psi_j(\bar{x}), \qquad \bar{w} = \sum_{j=1}^{N} W_j(t)\psi_j(\bar{x})$$

$$\phi = \sum_{j=1}^{N} \Phi_j(t)\Theta_j(\bar{x}) \tag{8}$$

where the overbar indicates nondimensionalization with respect to the wing span L and ψ_j, Θ_j are the jth normal modes of the associated linear structural model.

Let $\{q\}$ be a state vector that is defined as

$$\{q\} = \{\dot{V}_j, V_j, \dot{W}_j, W_j, \dot{\Phi}, \Phi_j, C_{ll}, C_{ml}, C_{dl}\}$$

where the structural mode number is $j = 1, 2, \ldots, N_s$ and the aerodynamic section number along the span of the wing is $l = 1, 2, \ldots, N_a$. Using the Galerkin method, one obtains a set of state-space matrix equations from Eqs. (1–6):

$$[\mathcal{A}]\{\dot{q}\} + [\mathcal{B}]\{q\} = \{F_0\}[\theta_0 + \alpha_G(t)] + \{F_N\} \tag{9}$$

Note that the coefficient matrices $[\mathcal{A}]$ and $[\mathcal{B}]$ are dependent on the flow and structural parameters. The force vectors $\boldsymbol{F}_0$ and $\boldsymbol{F}_N$ are (linear) static and gust loads obtained from the effects of steady and gust angle of attack and the nonlinear forces obtained from the structural nonlinearity and stall aerodynamics, respectively.

Equation (9) is a set of nonlinear equations of motion. A strictly linear flutter boundary is determined using Eq. (9) by setting $\boldsymbol{F}_N \equiv 0$ and $\theta_0 = 0$ and $\alpha_{G0} = 0$. There is no effect on the strictly linear flutter boundary of a preflutter static deflection or initial conditions. For $\boldsymbol{F}_N \neq 0$, $\alpha_{G0} = 0$, and $\theta_0 \neq 0$, a large static preflutter deformation may exist, and then a dynamic perturbation approach is used to determine the small perturbation flutter boundary of this nonlinear system about a nonlinear and nontrivial static equilibrium condition. That is, one assumes

$$q = \bar{q} + \hat{q} \tag{10}$$

where the overbar refers to the static equilibrium value of the variable, and corresponding quantities with a caret are small (linear) dynamic perturbations about the static equilibrium state.

When Eq. (10) is substituted into Eq. (9), a set of static equilibrium equations and dynamic perturbation equations is obtained. The static equilibrium equations comprise a set of nonlinear algebraic equations for the unknown state vector $\{\bar{q}\}$.

The dynamic perturbation equations about a static equilibrium state are

$$[\bar{\mathcal{A}}]\{\dot{\hat{q}}\} + [\bar{\mathcal{B}}]\{\hat{q}\} = \{0\} \tag{11}$$

Note the coefficient matrices $[\bar{\mathcal{A}}]$ and $[\bar{\mathcal{B}}]$ are dependent on the flow velocity and the static equilibrium state, for example, U, $\bar{q}$, etc.

On the other hand, to determine the gust response of this aeroelastic system, we use Eq. (9) and a time-marching approach, that is, a Runge–Kutta method (see Ref. 6).

Correlation Between Theory and Experiment

Results Without Gust Loads

A brief discussion of these results is included here as background for the subsequent presentation of the results for gust response. These results serve to calibrate the intrinsic dynamics of the aeroelastic model.

Static Aeroelastic Deflections of the Wing

Typical theoretical and experimental results are shown in Figs. 3a and 3b for a steady angle of attack, $\theta_0 = 1$ deg. Figure 3a is for the tip flap wise deflection and Fig. 3b for the tip twist. The solid line indicates the theoretical results, and the bar indicates the measured data. The experimental data appear to have some scatter due to the turbulent aerodynamic flow, although the flow noise is small. A very high measurement sensitivity is obtained from the mirror technique. A bar is used in Fig. 3 to indicate the magnitude of the experimental response uncertainty. As shown Fig. 3, both the tip and twist deflection increase with increasing flow velocity. The theoretical prediction and measured data in Fig. 3 are acquired before the onset of flutter and LCO. In general, the agreement between theory and experiment is good, that is, within 10% or less. In the higher-flow-velocity range, the data fluctuation increases due to greater aerodynamic turbulence. The experimental LCO data will be discussed in the next section.

Flutter and LCO Response

Very clear flutter and LCO response are observed in the present wind-tunnel test. Experimental flutter and LCO response are determined for four different steady angles of attack, that is, $\theta_0 = 0$, 0.25, 0.5, and 0.7 deg. For the safety of this wing model, we did not determine flutter or LCO for $\theta_0 > 0.7$ deg. The theoretical results are obtained from the dynamic perturbation Eq. (11) and also using a time-marching approach for the full nonlinear Eq. (9). For no static wing deformation, the strictly linear flutter speed and frequency are found to be 33.8 m/s and 22 Hz, respectively.

Figure 4 shows the dynamic perturbation flutter velocity (Fig. 4a) and frequency (Fig. 4b) vs the steady angle of attack from both theory and experiment. The solid line is for the dynamic perturbation solution and the filled circle is for the experimental data (onset velocity of flutter or LCO). The flutter velocity increases as the steady angle of attack increases. This is because the torsional natural frequency increases with increasing the static flapwise deflection.[5] The maximum difference between theory and experiment is only about 2%. The experimental flutter frequency is lower than that from the theory. The maximum difference is about 5%. For larger θ_0, the more refined theoretical model of Patil et al.[3] might give better agreement with the experimental data, and this is a worthy subject of further study.

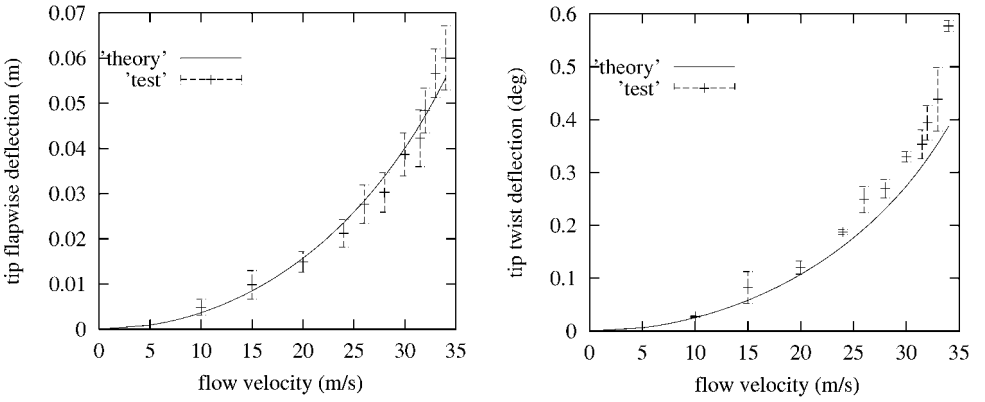

a) Flap **b) Twist**

Fig. 3 Static aeroelastic deflections of the wing vs flow velocity for steady angle of attack θ_0 = 1 deg.

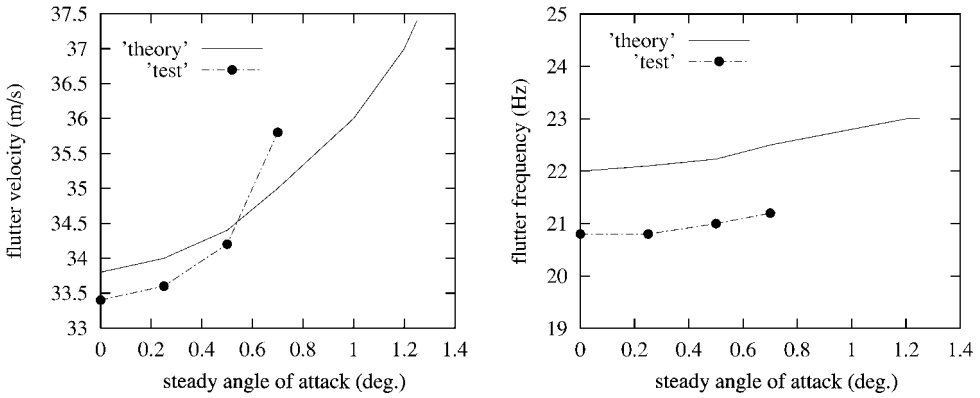

a) Flutter velocity b) Flutter frequency

Fig. 4 Perturbation eigenvalue solution of the nonlinear aeroelastic system vs steady angle of attack at the root section.

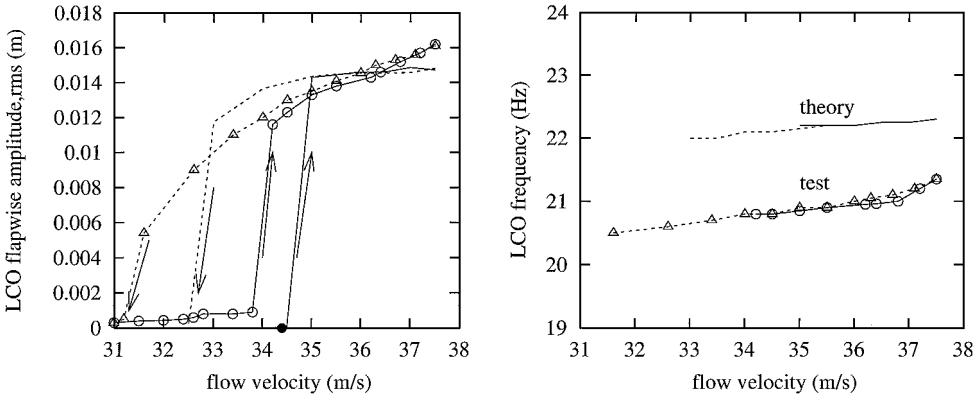

a) Amplitude b) Frequency

Fig. 5 Midspan LCO vs flow velocity for θ_0 = 0.5 deg.

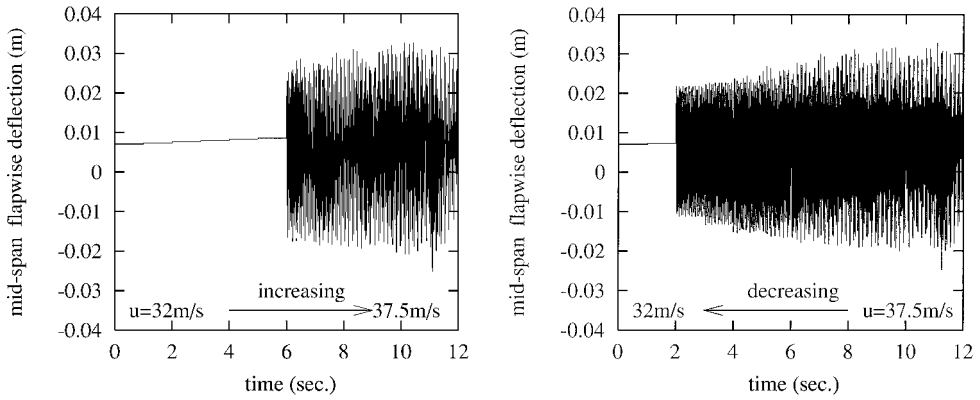

a) Increasing flow velocity b) Decreasing flow velocity

Fig. 6 LCO time history for θ_0 = 0.5 deg at midspan.

Typical LCO amplitude and frequency vs flow velocity for $\theta_0 = 0.5$ deg and at the midspan position are shown in Figs. 5a and 5b, respectively. The theoretical and experimental amplitudes are taken as rms average values from a 50-s sampling interval. The open circles and triangles indicate the experimental results for increasing and decreasing flow velocity, respectively. The solid and broken lines (without symbols) indicate the theoretical results for increasing and decreasing flow velocity, respectively. The symbol filled circle indicates the linear flutter velocity that is calculated from the perturbation eigenvalue solution. For the increasing flow velocity case, the theoretical LCO occurs when the flow velocity is larger than the perturbation flutter velocity and the amplitude has a jump from almost rest to a larger value. Once the onset of LCO occurs, the amplitude increases smoothly with increasing the flow velocity. When $U > 37.5$ m/s, a numerical or possibly a physical diverging time history is found in the theoretical model. For the case of decreasing flow velocity, as shown by the broken line, the LCO amplitude decreases but does not exactly coincide with those for the increasing velocity case. Also there is a jump in the LCO response at $U = 33$ m/s, which is a distinctly lower velocity than that found for the increasing velocity case, that is, $U = 35$ m/s.

To show further details of the theoretical results, two time history figures have been prepared for the LCO responses obtained from increasing or decreasing flow velocity. The results are shown in Figs. 6a and 6b for $\theta_0 = 0.5$ deg. Figure 6a is the result from increasing velocity, and Fig. 6b is for decreasing velocity. There are 12 flow velocities from $U = 32$ to 37.5 m/s with $\Delta U = 0.5$ m/s considered in the calculation. At each flow velocity, the time history is computed until the system achieves a steady-state LCO response. In general, it takes about 20 s (a time step of $\Delta t = 1/2048$ s is used).

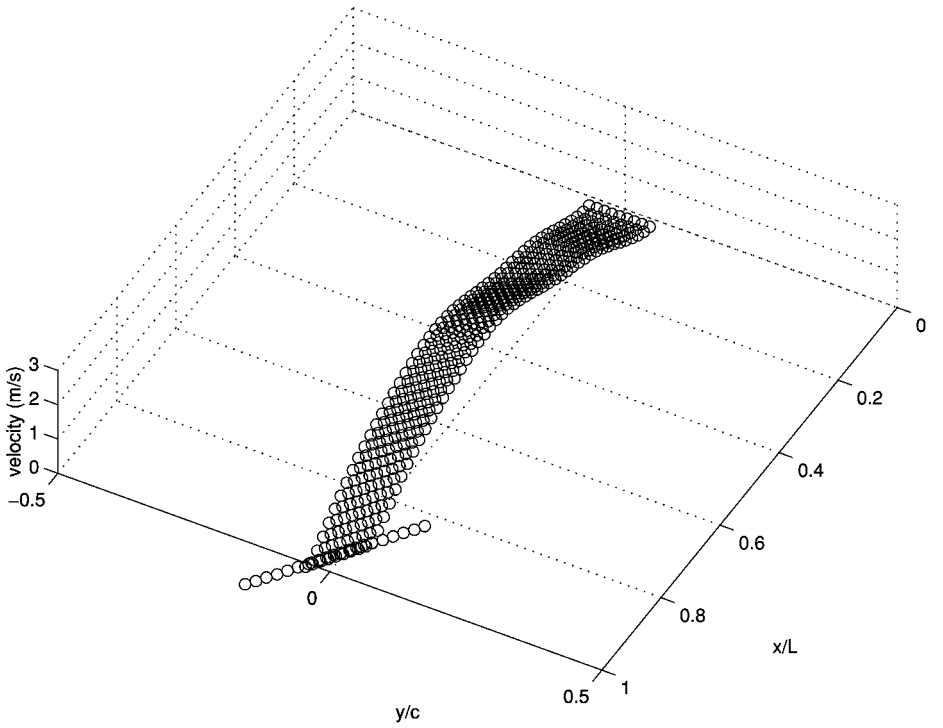

Fig. 7 Theoretical LCO vibration mode shape for U = 35 m/s and θ_0 = 0.5 deg.

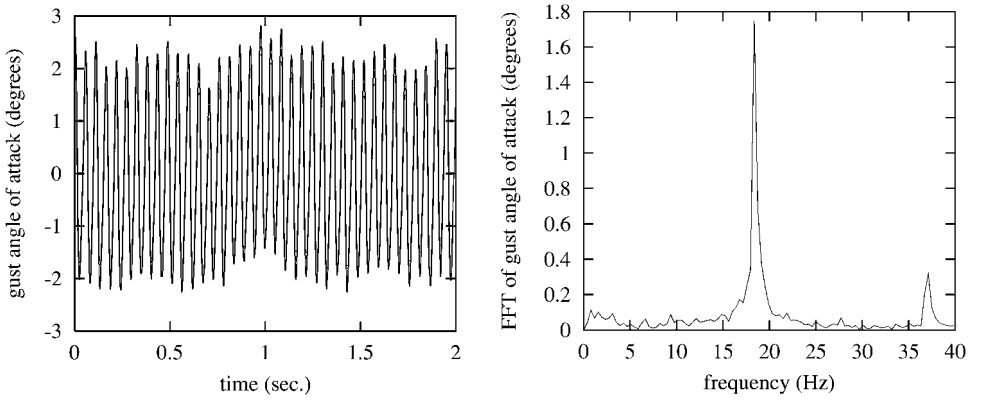

a) Time history **b) FFT analysis**

Fig. 8 Single harmonic gust excitation for U = 25 m/s and gust frequency ω = 18.5 Hz.

In Fig. 6a, the LCO response is shown in time intervals of 1 s for the several flow velocities. For each flow velocity (increasing ΔU), the initial conditions used are provided by the previous LCO state. For decreasing velocity, the results are shown in Fig. 6b. Again hysteresis in the response is seen depending on whether the flow velocity is increasing or decreasing.

In the experimental measurement, two different LCO responses are also observed for increasing and decreasing flow velocity. With increasing flow velocity, a jump at $U = 33.8$ m/s is found, which is similar to the theoretical results at $U = 34.3$ m/s as shown by the open circle with a solid line in Fig. 5a. This velocity at this jump is called the experimental flutter velocity. As the flow velocity increases further, the LCO amplitude measured has a modestly larger increase than that found from theory. When the flow velocity is decreased, another jump is found at $U = 31.4$ m/s as shown in Fig. 5a and as indicated by the open triangle with a broken line. The experimental LCO amplitudes for decreasing velocity are modestly smaller than those found for increasing velocity.

The LCO frequency vs flow velocity is shown in Fig. 5b. The symbols used are the same as those for Fig. 5a. As shown in Fig. 5b, the LCO frequency has a slight change as the flow velocity increases. The theoretical/experimental agreement is reasonably good, for example, about 5% for LCO frequency and even closer for LCO amplitude. The difference between theory and experiment for the flow velocities at which the jumps occur is also less than 5%.

Hence, a hysteresis phenomenon was found from both the theoretical prediction and experimental observation in the present vertically mounted wing model. As shown in Ref. 6 for a horizontally mounted wing, the stall aerodynamic nonlinearity is responsible for this hysteresis and LCO behavior.

The LCO vibration mode shape is similar to the flutter mode, with the most important coupling occurring between the first torsion mode and second flap mode. Figure 7 shows the theoretical LCO mode shape along the wing elastic axis for $U = 35$ m/s and $\theta_0 = 0.5$ deg.

The preceding results are closely comparable to those of Ref. 6, even though the experimental models are differently mounted. Hence, there is a sound basis for now considering gust load excitation.

Results with Gust Loads

To obtain a more meaningful correlation between theory and experiment, the gust angles of attack for both harmonic and frequency sweep gust excitations are measured and quantitatively calibrated. For a single harmonic gust, a typical time history and corresponding fast Fourier transform (FFT) analysis of the gust angle of attack are shown in Figs. 8a and 8b for $U = 25$ m/s and gust frequency $\omega = 18.5$ Hz. As shown in the FFT analysis of Fig. 8b, the gust load is not a pure sinusoid. The second harmonic component cannot

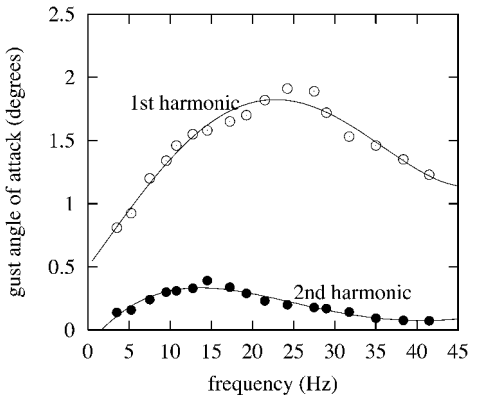

Fig. 9 Gust angle of attack vs gust frequency for U = 25 m/s: experimental data points are indicated by circles, and solid lines are curve fits.

be neglected. Similar results are found for other gust frequencies. Figure 9 shows the measured gust angle of attack α_G vs gust excitation frequency (hertz) for a flow velocity of $U = 25$ m/s. In Fig. 9, an open circle indicates the measured first harmonic component and the filled circle indicates the second harmonic component. The solid line is a least-square curve fitting of the experimental data. A formula based on the measured experimental gust angle of attack is constructed as

$$\alpha_G(t) = \bar{\alpha}_{G1} \sin \omega t + \bar{\alpha}_{G2} \sin(2\omega t + \Delta\phi) \tag{12}$$

where $\Delta\phi$ is a possible phase difference between first and second gust frequencies. However, it is difficult to determine $\Delta\phi$ due to the flowfield created by the present RSC gust generator. Thus, we assume $\Delta\phi = 0$ as an approximation.

Figure 10a shows a measured continuous linear frequency sweep gust angle of attack for $U = 25$ m/s. The gust strength (angle of

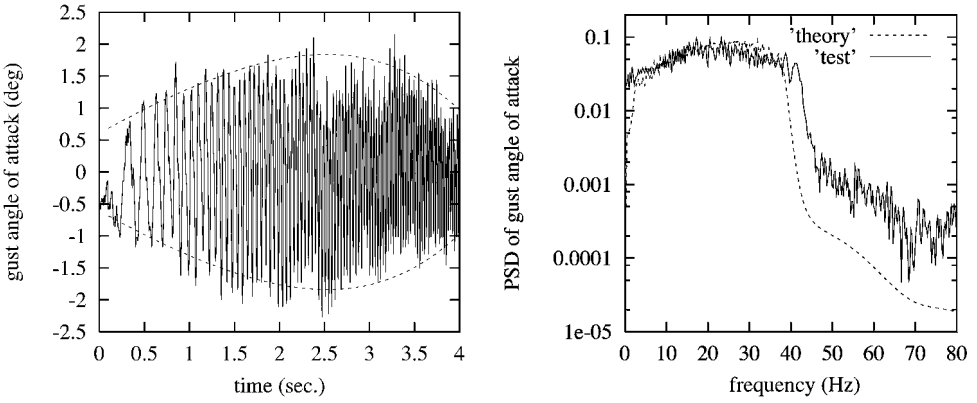

a) Time history **b) PSD analysis**

Fig. 10 Frequency sweep gust excitation for U = 25 m/s.

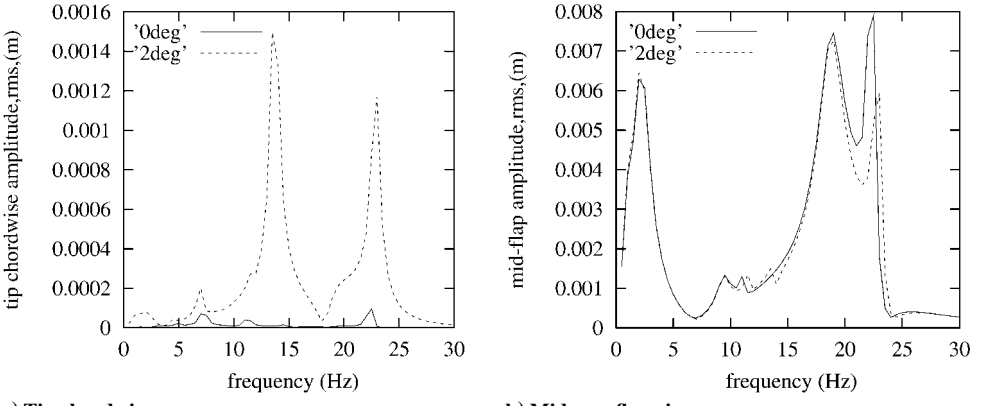

a) Tip chordwise **b) Midspan flapwise**

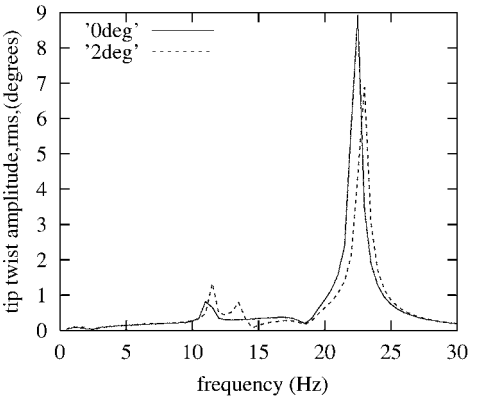

c) Tip twist

Fig. 11 Theoretical frequency response to harmonic gust for U = 25 m/s.

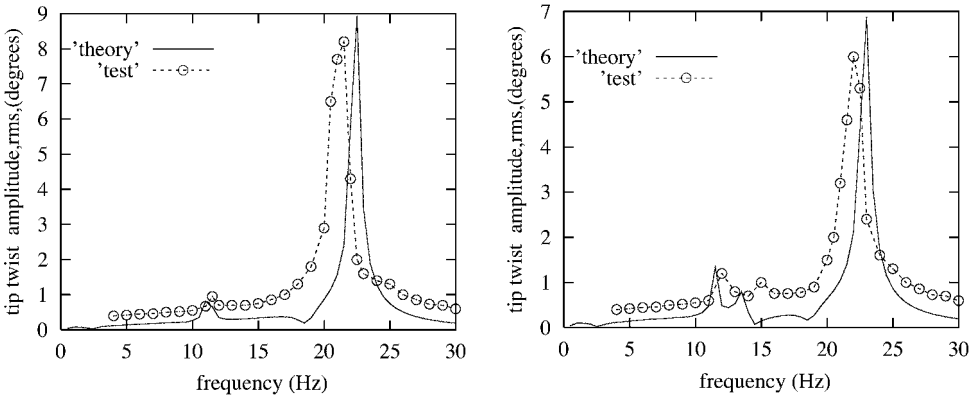

a) For $\theta_0 = 0$ b) For $\theta_0 = 2$ deg

Fig. 12 Theoretical and experimental tip twist response (rms) to gust excitation frequency for $U = 25$ m/s.

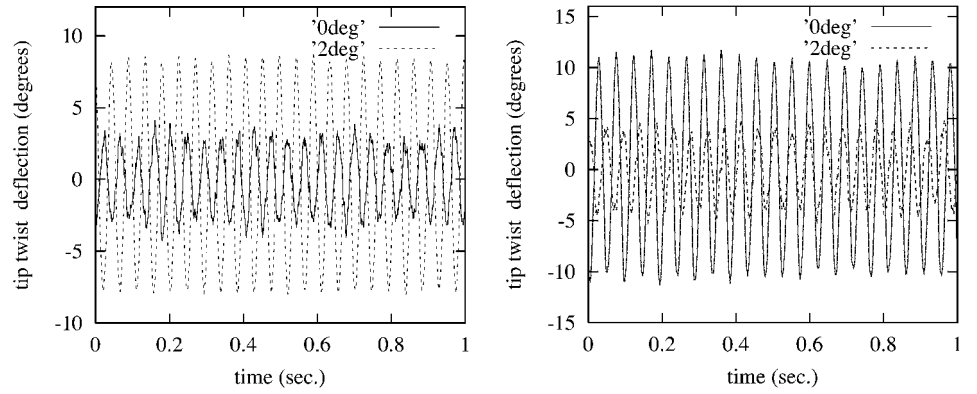

a) For $\omega = 22$ Hz b) For $\omega = 21$ Hz

Fig. 13 Measured time history of the tip twist deflection for $U = 25$ m/s, $\theta_0 = 0$, and $\theta_0 = 2$ deg.

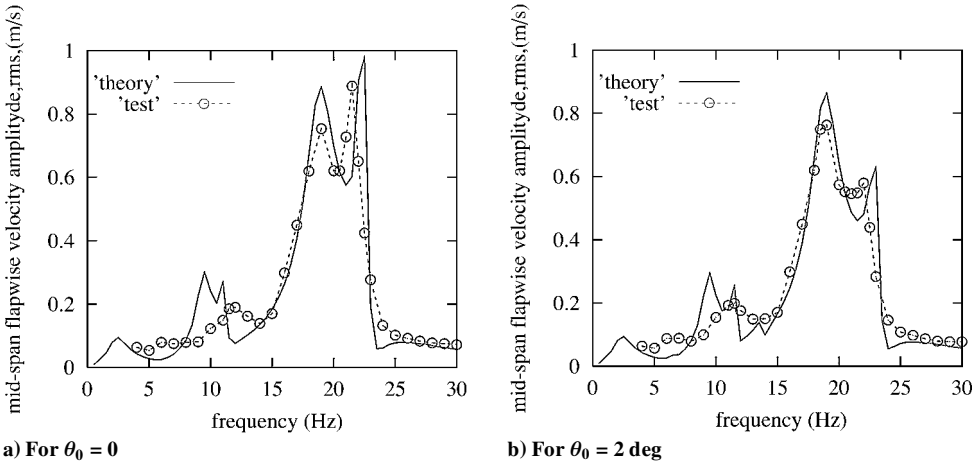

a) For $\theta_0 = 0$ b) For $\theta_0 = 2$ deg

Fig. 14 Theoretical and experimental velocity response (rms) to gust excitation frequency at midspan for $U = 25$ m/s.

attack) is not constant with time, as expected from theory. For the measured lateral gust, the minimum and maximum frequencies are 0 and 40 Hz, and the sweep duration T is 4 s. For convenient application in the gust response analysis, a formula based on experimental gust angle of attack data is constructed:

$$\alpha_G(t) = \bar{\alpha}_G(t)\sin\{\omega_1 + [(\omega_2 - \omega_1)/2T]t\}t \tag{13}$$

where $\alpha_G(t)$ is given by

$$\bar{\alpha}_G(t) = \sum_{i=0}^{4} c_i t^i \tag{14}$$

and $c_0, \ldots, c_4$ are determined by the least-square curve fitting method of the experimental data.

An envelope of the numerical gust simulation is plotted in Fig. 10a as indicated by the broken line.

Figure 10b shows a corresponding power spectra density (PSD) plot and comparison between the measured continuous linear frequency sweep gust (solid line) and the numerical gust simulation (broken line) for $U = 25$ m/s. The experimental PSD is based on an average over 20 sweep periods.

Equations (12) and (13) are used as theoretical gust excitations to calculate the nonlinear gust response for comparison with the experimental response results.

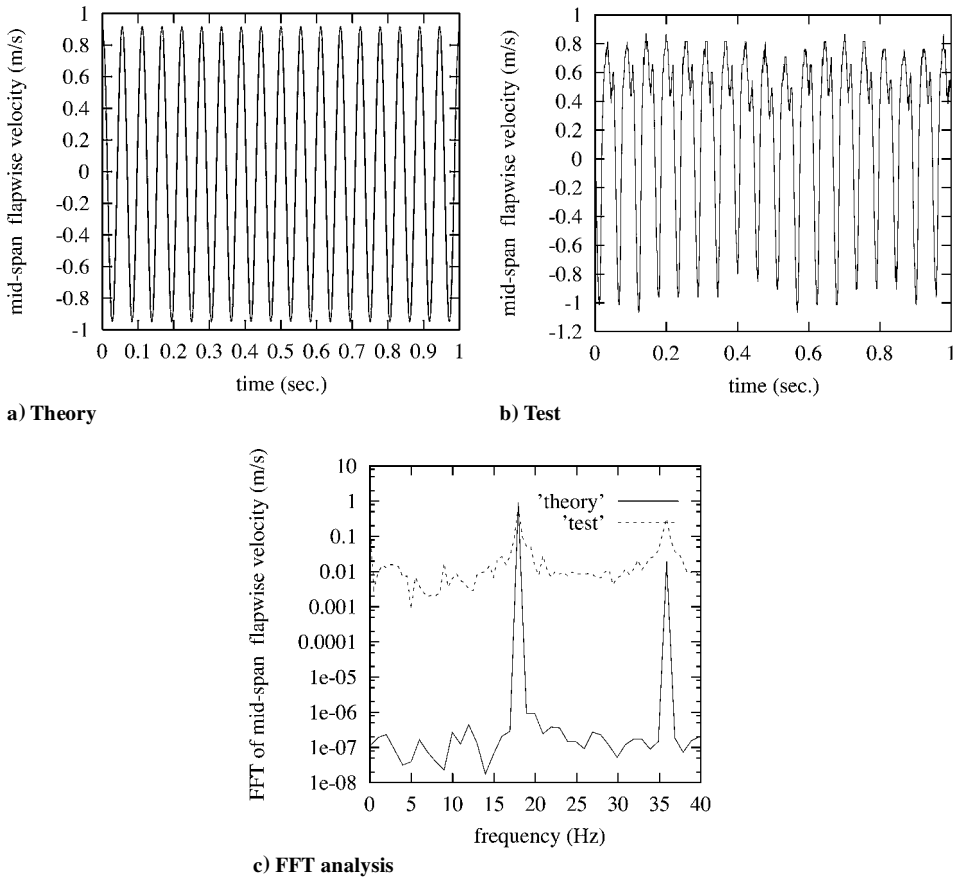

Fig. 15 Theoretical and experimental velocity time histories and FFT analysis at midspan for U = 25 m/s, θ_0 = 2 deg, and ω = 18 Hz.

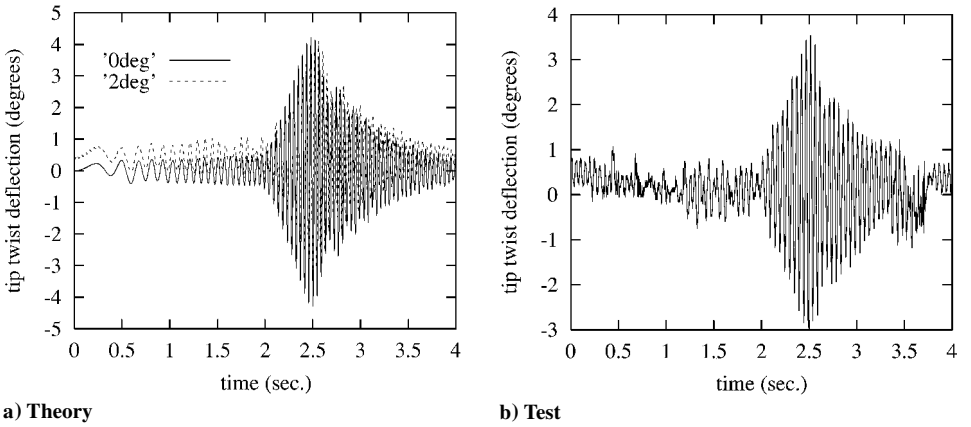

Fig. 16 Theoretical and experimental tip twist response to frequency sweep gust for U = 25 m/s and θ_0 = 0.

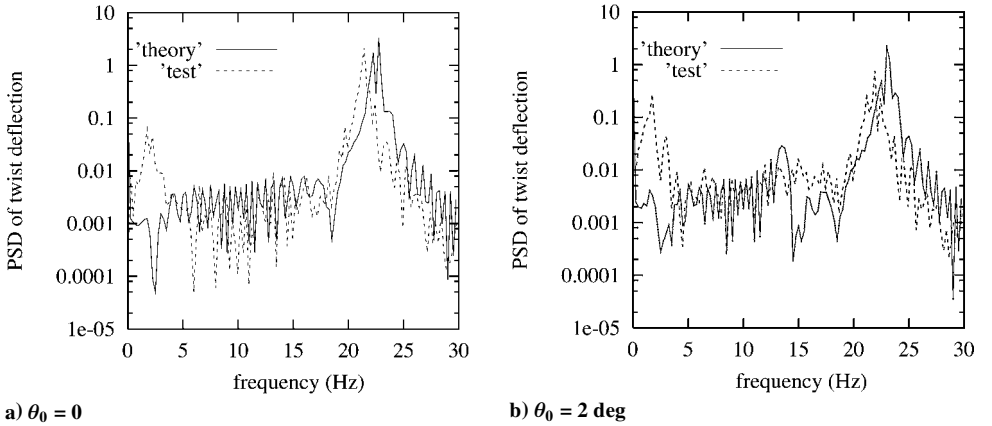

Fig. 17 Theoretical and experimental PSD of tip twist response to frequency sweep gust for U = 25 m/s.

Response to a Harmonic Gust Excitation

Equations (9) and (12) are used to calculate time-marching response and rms values obtained from the steady-state oscillation. The time step Δt is 1/2048. Usually, the steady state is reached after about 10 s. The duration of the transient response is largely determined by aerodynamic damping rather than structural damping for this model. Figure 11 shows the theoretical results for the gust response to harmonic excitation for a flow velocity of $U = 25$ m/s and a steady angle of attack, $\theta_0 = 0$ and 2 deg. Figure 11a shows the tip chordwise rms amplitude, Fig. 11b shows the midspan flapwise amplitude response, and Fig. 11c shows the tip twist. The responses for $\theta_0 = 0$ and 2 deg are indicated by the solid and broken lines, respectively. Note that for a linear theory, there is no effect of θ_0 on the results. Hence, the differences between the results for $\theta_0 = 0$ and 2 deg is a measure of the nonlinear effects.

As shown in Fig. 11a for the chordwise response, there is a very small response amplitude for the $\theta_0 = 0$ deg. This is because the airfoil drag itself is small. When $\theta_0 = 2$ deg, the chordwise response becomes larger, particularly near the first chordwise and torsional natural frequencies ($\omega_v = 14.25$ Hz and $\omega_\phi = 24.5$ Hz). The chordwise excitation is dominated by the chordwise component of the lift.

As shown in Fig. 11b for the midspan flapwise response, there are three dominant peaks corresponding to the first and second flapwise natural frequencies ($\omega_{f1} = 2.62$ Hz and $\omega_{f2} = 18.25$ Hz) and first torsional natural frequency. For the gust responses near the two flapwise natural frequencies, there is a slight difference between $\theta_0 = 0$ and 2 deg. This is because the large static flapwise deflection generates a slight change of the flapwise natural frequency.[5] Note that the tip flapwise deflection for $\theta_0 = 2$ deg and $U = 25$ m/s is 0.03 m. However, the torsional natural frequency is more dependent on the static flapwise deflection than the flap natural frequency. The gust response near the torsional frequency has a larger change with θ_0 both in response amplitude and peak frequency. Such results are also seen from Fig. 11c for tip twist response amplitude. The torsional frequency of this aeroelastic system increases with θ_0. It is believed this is because of the larger static flapwise deflection ($\theta_0 = 2$ deg), which increases the structural torsional natural frequency.

Figure 12 shows the correlation between the theoretical and experimental results for the tip twist response (rms) vs gust excitation frequency at a flow velocity of $U = 25$ m/s. Figure 12a is for $\theta_0 = 0$ and Fig. 12b is for $\theta_0 = 2$ deg. In Figs. 12, an open circle with the broken line indicates the measured data and the solid line indicates the theoretical results. The dominant response is near the torsional natural frequency. The correlation is reasonable except for a frequency difference at the peak amplitude. The difference between theory and experiment for the peak frequency is about 7.5%.

When Fig. 12a is compared to Fig. 12b, it is found the resonance frequency of this aeroelastic system increases (for both theoretical and experimental results) when θ_0 increases from 0 to 2 deg. Experimental time histories are shown in Fig. 13a for a gust frequency, $\omega = 22$ Hz, and in Fig. 13b for $\omega = 21$ Hz. In Figs. 13, the solid

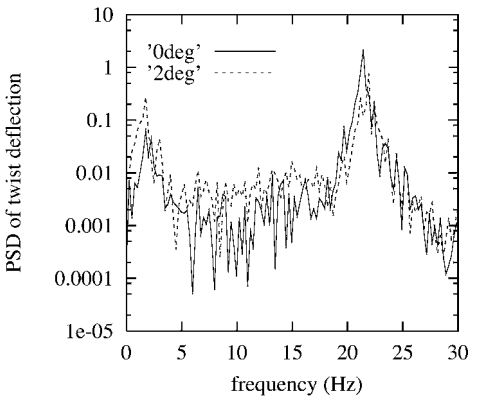

Fig. 18 Experimental PSD of tip twist response to frequency sweep gust for U = 25 m/s, θ_0 = 0, and 2 deg.

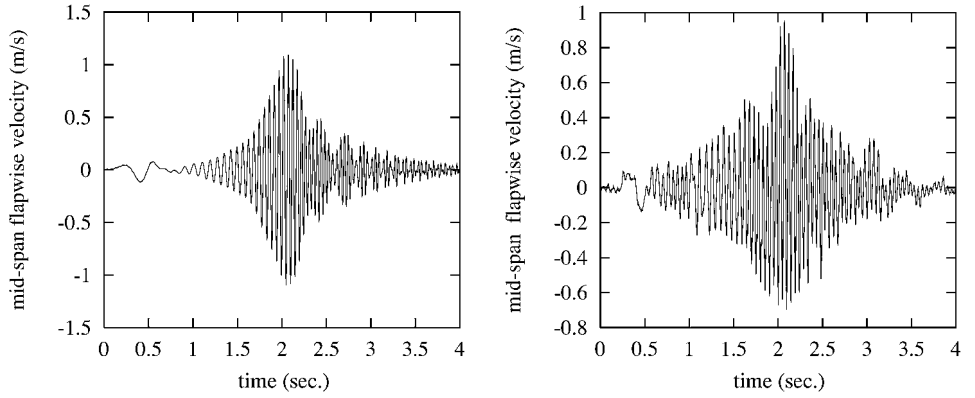

a) Theory **b) Test**

Fig. 19 Theoretical and experimental flapwise velocity response at the midspan to frequency sweep gust for U = 25 m/s and θ_0 = 2 deg.

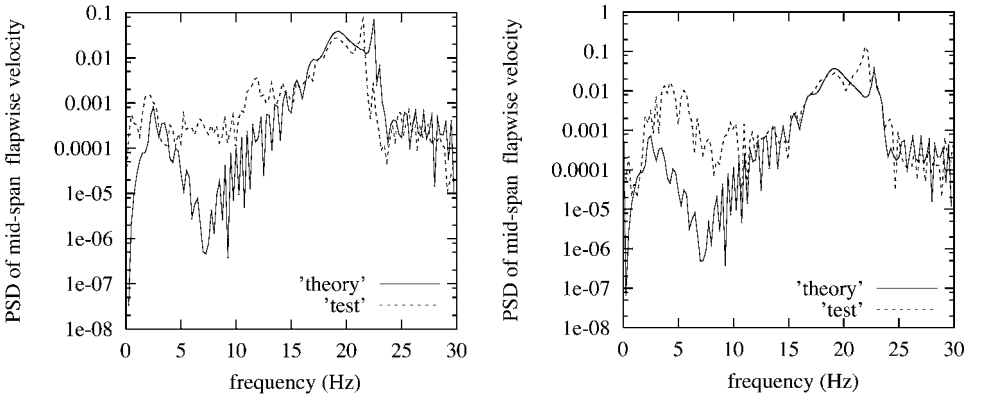

a) θ_0 = 0 **b) θ_0 = 2 deg**

Fig. 20 Theoretical and experimental PSD of flapwise velocity response at the midspan to frequency sweep gust for U = 25 m/s.

line is from $\theta_0 = 0$ and the broken line is from $\theta_0 = 2$ deg. As shown in Fig. 13a, when $\omega = 22$ Hz, there is a large twist deflection for $\theta_0 = 2$ deg, but a small twist deflection for $\theta_0 = 0$. When $\omega = 21$ Hz, the results are reversed, as shown in Fig. 13b.

A similar correlation between the theoretical and experimental results for the midspan velocity response (rms) vs gust excitation frequency at the flow velocity $U = 25$ m/s is shown in Fig. 14a ($\theta_0 = 0$) and Fig. 14b ($\theta_0 = 2$ deg). Two dominant peaks are found. One is at frequency 19 Hz, which corresponds to the second flapwise bending mode, and the other is near 22–23 Hz, which corresponds to the first torsional mode. The theoretical and experimental results verify that for the bending mode, the resonance frequency is almost independent of θ_0. However, for the torsion mode, the resonance frequency increases with θ_0. The correlation is good. A typical comparison of theoretical and measured time histories for $U = 25$ m/s, $\theta_0 = 2$ deg, and $\omega = 18$ Hz are shown in Fig. 15a (theory) and Fig. 15b (test), respectively. A theoretical and experimental FFT analysis that corresponds to Figs. 15a and 15b is shown in Fig. 15c. As shown in Fig. 15c, the dominant response component is at the gust excitation frequency, but the second harmonic response component is not very small, especially for the measured data. The natural turbulence in the wind tunnel is not modeled in the theory; hence, the difference in the off-peak responses in Fig. 15c between theory and experiment.

Response to a Frequency Sweep Gust Excitation

Equations (9) and (13) are used to calculate time histories and PSD due to a frequency sweep gust. The theoretical and experimental results for tip twist response are shown in Figs. 16a and 16b for a flow velocity of $U = 25$ m/s and a steady angle of attack, $\theta_0 = 0$ deg. There are 10 sweep periods in 40 s and the total sampling length is 51,200 points for the measured data. Figure 16b is one sweep period of the total sampling length. Theoretical (solid line) and experimental (dashed line) PSD results that corresdpond to Figs. 16a and 16b are shown in Figs. 17a ($\theta_0 = 0$) and 17b ($\theta_0 = 2$ deg) for an average over 10 sweep periods. The results are very similar to Figs. 12a and 12b. It further confirms our earlier conclusions.

To observe the effect of the steady angle of attack θ_0 on the aeroelastic frequency, a comparison between two experimental PSD of the tip twist for $\theta_0 = 0$ and 2 deg is shown in Fig. 18. It verifies experimentally our earlier conclusion in Ref. 6 regarding the effect of θ_0.

Figures 19a and 19b show the theoretical and experimental time histories of the mid-span flapwise velocity response for a flow velocity of $U = 25$ m/s and a steady angle of attack, $\theta_0 = 2$ deg. Theoretical (solid line) and experimental (dashed line) PSD results that correspond to Figs. 19a and 19b are shown in Fig. 20a ($\theta_0 = 0$) and 20b ($\theta_0 = 2$ deg). The agreement between theory and experiment is reasonably good.

Conclusions

The present experimental and theoretical results provide new insights into nonlinear aeroelastic phenomena for high-aspect-ratio wings (with a tip slender body) that have a beamlike structural behavior. As previously noted,[2–6] the effects of the geometric structural nonlinearity depend on the ratio of the flap and chordwise bending stiffnesses, EI_2/EI_1. For relatively small EI_2/EI_1, the flutter instability boundary has only a small change due to the structural nonlinearity and preflutter static deformation. This earlier conclusion has also been confirmed by theoretical calculations for the frequency response to both a harmonic and a frequency sweep gust. These results were used to select the bending stiffness ratio for the experiment reported here.

The fair to good quantitative agreement between theory and experiment for gust response verifies that the present mathematical model and method has reasonable accuracy for a range of nonlinear gust response analysis.

The primary variable used to induce nonlinearity in the present experiment was the steady angle of attack at the wing root. This in turn induces a static nonlinearity that changes the dynamic characteristics of the wing and, hence, its response to gust excitation. However, the dynamic response levels arising from the gust excitation in the present experiment are themselves relatively small. Hence, dynamic nonlinearities per se in the gust response are thought to be modest in the tests reported here.

Future work might be directed toward 1) large gust excitations to induce nonlinear dynamic response, 2) consideration of gust response in the flow velocity range where LCO also occurs, and 3) calculations with improved structural models that are appropriate to larger deflections such as those developed by Patil et al.[2,3] and Patil and Hodges.[5]

Acknowledgments

This work was supported by the Defense Advanced Research Projects Agency through Air Force Office of Scientific Research Grant F49620-99-1-00253, "Aeroelastic Leveraging and Control Through Adaptive Structures," under the direction of Ephrahim Garcia and Dan Segalman. All numerical calculations were done on a supercomputer, T916, in the North Carolina Supercomputing Center. We would also like to thank our colleague, Robert Clark, for useful discussion of this work.

References

[1] Hodges, D. H., and Dowell, E. H., "Nonlinear Equations of Motion for the Elastic Bending and Torsion of Twisted Nonuniform Rotor Blades," NASA TN D-7818, 1974.

[2] Patil, M. J., Hodges, D. H., and Cesnik, C. E. S., "Nonlinear Aeroelastic Analysis of Complete Aircraft in Subsonic Flow," *Journal of Aircraft*, Vol. 37, No. 5, 2000, pp. 753–760.

[3] Patil, M. J., Hodges, D. H., and Cesnik, C. E. S., "Limit Cycle Oscillations in High-Aspect-Ratio Wings," *Journal of Fluids and Structures*, Vol. 15, No. 1, 2001, pp. 107–132.

[4] Tang, D. M., and Dowell, E. H., "Effects of Geometric Structural Nonlinearity on Flutter and Limit Cycle Oscillations of High-Aspect Ratio Wings," *Journal of Fluids and Structures* (submitted for publication).

[5] Patil, M. J., and Hodges, D. H., "Importance of Aerodynamic and Structural Geometrical Nonlinearities on Aeroelastic Behavior of High-Aspect-Ratio Wings," AIAA Paper 2000-1448, 2000.

[6] Tang, D., and Dowell, E. H., "Experimental and Theoretical Study on Aeroelastic Response of High-Aspect-Ratio Wings," *AIAA Journal*, Vol. 39, No. 8, 2001, pp. 1430–1441.

[7] Tang, D. M., Paul, G. A., Cizmas and Dowell, E. H., "Experiments and Analysis for a Gust Generator in a Wind Tunnel," *Journal of Aircraft*, Vol. 33, No. 1, 1996, pp. 139–148.

[8] Tran, C. T., and Petot, D., "Semi-Empirical Model for the Dynamic Stall of Airfoils in View to the Application to the Calculation of Responses of a Helicopter Blade in Forward Flight," *Vertica*, Vol. 5, No. 1, 1981, pp. 35–53.

[9] Minguet, P., and Dugundji, J., "Experiments and Analysis for Composite Blades Under Large Deflections, Part II: Dynamic Behavior," *AIAA Journal*, Vol. 28, No. 9, 1990, pp. 1580–1588.

[10] Bisplinghoff, R. L., Ashley, H., and Halfman, R. L., *Aeroelasticity*, Addison Wesley Longman, Reading, MA, 1955, pp. 418–420.

[11] Tang, D. M., and Dowell, E. H., "Nonlinear Response of A Non-Rotating Rotor Blade to A Periodic Gust," *Journal of Fluids and Structures*, Vol. 10, No. 7, 1996, pp. 721–742.

C. Pierre
Associate Editor